Iron-Doped *Birch* Leaf-Derived Biopolymer-Based Zinc Oxide Nanocomposites: A Multifunctional Platform for Anticancer Activity and Imaging Applications against MCF-7 Cells

Sarojini. S[1], Dinesh Karthik. A[2*], Geetha. K[3],

[1]Chemistry Research Scholar, Shangmuga Industries Arts and Science College, Thiruvannamalai, Thiruvalluvar University, Vellore, Tamil Nadu, India.
Email: sarojini.jierah25@gmail.com.

[2*] Head, Associate Professor, Department of Chemistry, Shanmuga Industries Arts and Science College, Thiruvannamalai, Tamilnadu, India
Email: Dineshkarthik2008@gmail.com. (Corresponding Author)

[3] Head, Associate Professor, P.G & Research Department of Chemistry, Muthurangam Govt. Arts College, Vellore. Email: senthilkgeetha@gmail.com.

Abstract

Iron-doped zinc oxide nanocomposites (Fe-ZnO NCs), which are made from biopolymers derived from *birch* leaves, are presented in this work as a multipurpose platform for cancer theranostics that targets MCF-7 breast cancer cells. Successful iron incorporation was confirmed by characterization techniques (FTIR, XRD, HRTEM, HRSEM, EDX, and BET), which improved the surface, morphological, and structural characteristics. With a dose-dependent decrease in MCF-7 cell viability, Fe-ZnO nanocomposites demonstrated significant anticancer effects. At 200 µg/mL, viability was almost completely eradicated, dropping to about 10% from 20% for undoped ZnO. Significant disruption of the mitochondrial membrane potential and elevated ROS levels (roughly 1.5 times higher than undoped ZnO) further promoted apoptosis. Imaging studies demonstrated increased radiopacity in X-ray imaging (80 AU versus 10 AU for undoped ZnO), higher Hounsfield Units in CT imaging (450 HU versus 300 HU), and enhanced T2 relaxivity, reaching ~150 s^{-1} mM^{-1} at 10 mg/mL (compared to ~60 s^{-1} mM^{-1} for undoped ZnO). These results highlight Fe-ZnO NCs theranostic properties and their potential for *in vivo* cancer treatment and diagnosis.

Keywords: Iron-doped zinc oxide, Biopolymer-based nanocomposites, *Birch* leaf extract, MCF-7 breast cancer cells, Theranostics, Reactive oxygen species (ROS), Apoptosis, MRI contrast agent, X-ray imaging, CT imaging, Multifunctional platform.

1. INTRODUCTION

In recent years, zinc oxide (ZnO) nanocomposites have emerged as promising cancer treatment agents due to their inherent anticancer properties and versatility in biomedical applications [1]. These nanoparticles are particularly effective because of their biocompatibility, tunable properties, and ability to selectively induce cell death in cancer cells via the generation of reactive oxygen species (ROS), which can cause apoptosis while sparing healthy cells [2]. ZnO nanoparticles show significant promise for breast cancer treatment, particularly in MCF-7 cell models, as they target the cancerous cells' metabolism and oxidative stress pathways, providing a targeted approach to cancer therapy [3]. However, ZnO's full potential is frequently hampered by stability and a lack of multifunctionality in biological systems, prompting researchers to investigate ways to improve and broaden its biomedical applications.

In this context, biopolymer-based nanocomposites provide an environmentally friendly and sustainable alternative to nanoparticle synthesis, adding an extra layer of biocompatibility and functionalization to improve interaction with biological systems [4]. Natural biopolymers derived from plants, such as *birch* leaves, contain a wide range of bioactive compounds such as polyphenols and organic acids,

which act as natural reducing and stabilizing agents, promoting green nanomaterial synthesis [5]. By including biopolymer-based materials made from *birch* leaves, we can reduce the environmental impact of nanoparticle production while also improving the stability and bioactivity of ZnO nanocomposites. This approach is consistent with sustainable nanotechnology principles and meets the growing demand for environmentally friendly alternatives to nanomaterial synthesis.

One of the most difficult challenges in cancer treatment is developing multifunctional platforms that combine therapeutic and diagnostic capabilities, also known as theranostics [6-7]. Iron doping provides a unique solution to this problem by incorporating imaging functionalities into ZnO nanocomposites, thereby expanding their applications from therapeutic to theranostic. Iron, as a dopant, not only improves the magnetic properties of ZnO nanoparticles, but also expands their application as contrast agents in imaging modalities such as magnetic resonance imaging (MRI), X-ray, and computed tomography (CT) [8]. Because of their dual functionality, iron-doped ZnO nanocomposites can act as anticancer agents as well as imaging tools, allowing for real-time treatment monitoring and cancer therapy precision. These nanocomposites, which combine the therapeutic effect of ZnO with the diagnostic potential introduced by iron doping, represent an innovative approach to integrated cancer treatment and diagnosis. The selection of platforms based on leaf extracts for the synthesis of nanocomposites is the result of numerous research initiatives aimed at creating economical methods. Fe-doping is highlighted in recent research because of its imaging capabilities and possible uses in the treatment of cancer [9-11]. Motivated by these discoveries, we created a novel methodology for creating Fe-doped nanocomposites.

This study's objectives are divided into three areas: synthesis, therapeutic evaluation, and diagnostic potential. First, we intend to create iron-doped ZnO nanocomposites from *birch* leaf-derived biopolymers, leveraging the natural stabilizing agents found in *birch* leaves to support the green synthesis of stable, biocompatible nanoparticles. This eco-friendly approach is expected to produce nanoparticles with optimized size, morphology, and functional properties for biomedical applications. The second goal is to determine the anticancer activity of these nanocomposites on the MCF-7 breast cancer cell line. This assessment will include cytotoxicity, cell viability, ROS production, and apoptosis tests to determine the nanoparticles' specific impact on breast cancer cells. Finally, the study intends to evaluate the iron-doped nanocomposites' potential as contrast agents in MRI, X-ray, and CT imaging. The magnetic properties imparted by iron doping are expected to improve T1 and T2 relaxation times in MRI, attenuation in X-ray, and contrast efficiency in CT imaging, demonstrating their multifunctional utility across multiple imaging modalities.

Our central hypothesis is that Fe-ZnO NCs will not only improve their anticancer properties by producing more ROS, but will also function as effective contrast agents, making them suitable for theranostic applications. Iron doping is expected to improve ZnO nanoparticles' selective toxicity toward cancer cells, while the magnetic properties of iron will make the nanoparticles visible under MRI and other imaging techniques, allowing for precise localization and monitoring of cancerous tissues. This method provides an integrated platform for concurrent treatment and diagnostic imaging, which represents a significant advancement in the development of multifunctional nanocomposites for cancer theranostics.

2. MATERIALS AND METHODS

2.1 Materials

The materials used to synthesize Fe-ZnO NCs were obtained from reputable suppliers to ensure high quality and reproducibility during the synthesis process. *Birch* leaf powder, rich in natural biopolymers, was purchased from a local organic shop in Thiruvannamalai, Tamilnadu. This powder was the primary source for extracting biopolymer, which acted as a stabilizing and capping agent in the synthesis, in accordance with green chemistry principles. Fisher Scientific laboratory chemicals, provided zinc nitrate hexahydrate ($Zn(NO_3)_2 \cdot 6H_2O$) and iron nitrate nonahydrate ($Fe(NO_3)_3 \cdot 9H_2O$). Zinc nitrate

hexahydrate was chosen for its stability and suitability in nanoparticle synthesis, whereas iron nitrate nonahydrate provided a consistent iron source for doping, which improved the anticancer and imaging properties of the ZnO nanocomposites. Additional chemicals included sodium hydroxide (NaOH) from Sigma-Aldrich for pH control of nanoparticle formation, and ethanol from Fisher Scientific for biopolymer extraction.

2.2. Synthesis of *Birch* Leaf-Derived ZnO Nanocomposites

To produce zinc oxide nanocomposites (ZnO NCs) derived from *birch* leaf biopolymer, 10 g of *birch* leaf powder was mixed with 200 mL of ethanol or distilled water, and heat-assisted extraction was performed [12]. Following extraction, the solution was filtered to remove any remaining plant material, and the biopolymer was dried under reduced pressure to produce a stable powder. To synthesize ZnO nanocomposites, combine a 10 mM aqueous solution of zinc nitrate hexahydrate ($Zn(NO_3)_2 \cdot 6H_2O$) with 5 g of biopolymer extract. The reaction was carried out under optimal conditions, with pH (adjusted with 1 M NaOH), temperature (maintained at 80°C), and zinc precursor concentration all under control. These conditions favoured the formation of ZnO NCs, with NaOH supplying hydroxide ions that aid in ZnO nucleation and growth. The reaction was heated for 2 hours to control particle size, as higher temperatures typically result in smaller, more evenly distributed nanoparticles [13]. This green synthesis method uses biopolymers to produce stable, uniform ZnO NCs that can be further functionalized.

2.3. Preparation of Fe-Doped *Birch* Leaf-Derived ZnO Nanocomposites

To improve the therapeutic and diagnostic potential of the ZnO nanocomposites, 5 wt% iron (Fe) doping was applied. Iron nanoparticles (Fe NPs) were synthesized separately by reducing 10 mM iron nitrate nonahydrate ($Fe(NO_3)_3 \cdot 9H_2O$) with a mild reducing agent, such as sodium borohydride ($NaBH_4$), under controlled conditions to ensure well-defined particle formation [14]. The Fe NPs were then incorporated into the 5% ZnO NCs solution using either in-situ doping during ZnO synthesis. In the in- situ doping approach, 0.5 g of Fe NPs were added to the reaction mixture during ZnO synthesis, resulting in homogeneous dispersion within the ZnO matrix and improved magnetic and anticancer properties. Alternatively, in post-synthesis doping, Fe NPs were introduced onto the surface of ZnO nanocomposites with 20 mL of Fe NPs suspension, potentially increasing their surface reactivity for imaging purposes. The resulting Fe-doped ZnO nanocomposites (Fe-ZnO NCs) are typically light brown to pale yellow in colour solution due to the presence of iron within the ZnO matrix. This was dried at 80°C for 4-5 hrs in microwave oven. A brownish black colour powder called Fe-ZnO NCs was obtained. The synthesized Fe- ZnO NCs were carefully dried and stored in an airtight container at room temperature for later use. The overall preparation process is depicted in Figure 1.
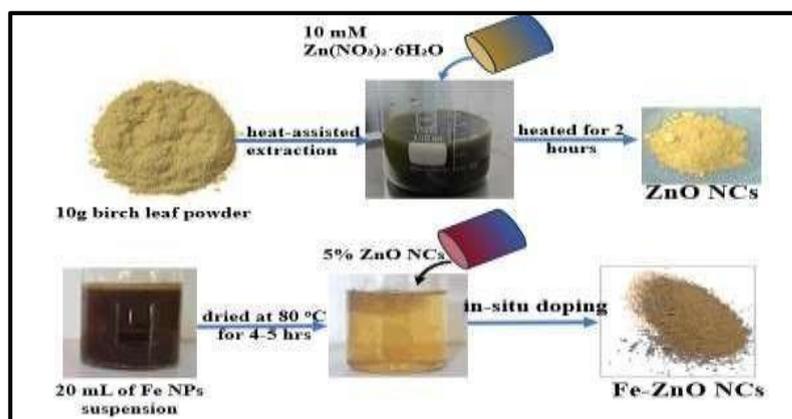

Fig 1: Schematic diagram depicting the overall synthesis of ZnO NCs from *Birch* leaf and Fe Doped ZnO NCs

2.5. Characterization of Nanocomposites

The structural, morphological, and functional properties of Fe-ZnO NCs were thoroughly investigated. The functional groups of ZnO were confirmed using FTIR, which also identified the Fe and ZnO composition blended with Fe-ZnO NCs synthesis. XRD was used to investigate structural properties and functional groups, confirming ZnO's crystalline structure and identifying any phase changes caused by iron doping. HRTEM and HRSEM analyses were critical for determining particle size, shape, and surface morphology, with TEM providing nanoscale resolution on individual particles and HRSEM providing insights into aggregate formations. The surface area and pore size distribution were determined using Brunauer-Emmett-Teller (BET) analysis, which is critical for understanding the potential for high surface interaction with cancer cells and imaging agents. MTT assay and ROS generation potential were evaluated, as they play an important role in the anticancer activity of ZnO nanoparticles, with higher ROS levels correlated with increased cytotoxicity in cancer cells. Additionally, Multimodal Imaging techniques were used to determine the imaging potential of Fe-ZnO NCs.

2.6. *In Vitro* Anticancer Activity

2.6.1. Cell Culture

The MCF-7 breast cancer cell line, a well-known model in breast cancer research, was chosen to assess the anticancer potential of Fe-ZnO NCs due to its susceptibility to apoptosis-inducing agents [15]. Cells were cultured under standard conditions, such as 37°C, 5% CO_2 atmosphere, and high humidity for optimal growth. For treatment studies, cells were seeded at an optimal density in 96-well plates, allowing for controlled exposure to different concentrations of iron-doped ZnO nanocomposites. Nanocomposite concentrations (10-200 μg/mL) were tested for their dose-dependent cytotoxic effects on MCF-7 cells [16]. This setup provided a controlled and reproducible environment for determining the nanocomposites' therapeutic effects on cancer cells.

2.6.2. Cytotoxicity Assays

To determine the cytotoxic effects of Fe-ZnO NCs on MCF-7 cells, standard MTT or Alamar Blue assays were used. The MTT assay is widely used to assess cell viability by measuring mitochondrial activity; viable cells convert MTT into formazan, a purple-coloured product [17]. Alamar Blue, a resazurin-based assay, is another viable option for assessing cytotoxicity because it detects cell viability via colorimetric changes [18]. To compare treatments, cells were treated with varying concentrations of pure ZnO, iron- doped ZnO, and an untreated control group. The absorbance was measured with a microplate reader at the appropriate wavelength, and cell viability was calculated to determine the IC50 values (concentrations that inhibit 50% of cells) for each treatment group. This comparison revealed that iron-doped ZnO nanocomposites outperformed pure ZnO nanoparticles in terms of anticancer activity.

2.6.3. Apoptosis and ROS Assays

The mechanism of cell death induced by iron-doped ZnO nanocomposites was studied using apoptosis assays and ROS measurement. Apoptosis was detected using Annexin V-FITC/PI staining, a standard method for distinguishing between early and late apoptotic cells, and quantified using flow cytometry [19]. In this method, Annexin V-FITC binds to phosphatidylserine, which moves to the plasma membrane's outer leaflet during early apoptosis, whereas propidium iodide (PI) stains cells with compromised membranes during late apoptosis or necrosis. Flow cytometry data allowed for the quantification of apoptotic populations, which provided insight into the nanocomposites' pro-apoptotic effects on MCF-7 cells. Furthermore, intracellular ROS levels were measured using ROS-sensitive fluorescent dyes, such as DCFH-DA, because increased ROS generation can trigger apoptosis by causing

oxidative stress in cells [20]. The relationship between ROS levels and cell death demonstrated that iron-doped ZnO nanocomposites cause cytotoxicity primarily via oxidative stress mechanisms.

2.7. Imaging Studies

2.7.1. Magnetic Resonance Imaging (MRI) Studies

The study sought to assess the efficacy of iron-doped ZnO nanocomposites as MRI contrast agents, specifically for T2-weighted imaging. MRI is highly sensitive to magnetic properties, so iron-based nanoparticles are particularly useful for imaging due to their paramagnetic behaviour, which induces strong T2 relaxation effects [21]. The relaxivity (r1 and r2) of the iron-doped ZnO nanocomposites was measured using a phantom model, which is a controlled environment that mimics tissue imaging conditions. The relaxivity values r1 (longitudinal) and r2 (transverse) were measured to determine their efficacy as contrast agents, as higher r2 values are typically associated with improved T2 contrast [22]. The MRI signal intensities from the Fe-doped ZnO nanocomposites were then compared to those of conventional agents, such as gadolinium-based agents, which are widely used but can pose safety risks. The expected result was improved T2-weighted contrast due to iron's magnetic nature, which could provide an alternative, potentially safer, and more effective MRI contrast option for diagnostic imaging.

2.7.2. X-ray Imaging Studies

The goal of the X-ray imaging studies was to investigate the radiopacity of iron-doped ZnO nanocomposites and determine their suitability as X-ray contrast agents. Radiopacity, or a substance's ability to absorb X-rays, is affected by the atomic number of the elements involved, with higher atomic numbers increasing X-ray attenuation [23]. Phantoms with varying concentrations of iron-doped ZnO nanocomposites were prepared and imaged using X-rays. Radiopacity was quantitatively analysed and compared to standard iodine-based X-ray contrast agents, which are widely used in medical imaging but have some limitations, such as hypersensitivity reactions [24]. The presence of iron in the ZnO matrix increases radio density, resulting in improved visibility under X-ray exposure. The findings of these studies could establish iron-doped ZnO nanocomposites as promising alternatives for safer, metal-based X-ray imaging.

2.7.3. CT Scan Imaging Studies

The CT scan imaging studies aimed to assess the ability of iron-doped ZnO nanocomposites to function as CT contrast agents. The Hounsfield Units (HU) used in computed tomography (CT) imaging measure tissue density differences. Given the higher atomic numbers of zinc and iron, these nanocomposites were expected to produce higher HU values, resulting in improved CT contrast [25]. In this section of the study, phantom models embedded with varying concentrations of iron-doped ZnO nanocomposites were imaged using CT. Hounsfield Units from these models were measured and compared to those from traditional contrast agents like iodine and barium compounds, which are widely used but can sometimes limit imaging quality due to poor contrast [26]. Enhanced contrast from the nanocomposites would indicate their suitability for CT imaging, introducing a new, biocompatible agent for better image quality. If proven effective, these nanocomposites could be used as multifunctional agents in MRI, X-ray, and CT imaging, improving diagnostic capabilities across modalities.

3. RESULTS AND DISCUSSION

3.1. Characterization Results

Fig 2 shows FTIR spectra of undoped ZnO and Fe-doped ZnO nanocomposites made from *birch* leaf-based biopolymers at 400 to 4500 cm^{-1}. The undoped ZnO spectrum shows Zn-O stretching vibrations around 440 cm^{-1} and a peak near 700 cm^{-1}, which may indicate Zn-O-Zn bonding. Furthermore, the spectrum shows an O-H bending mode around 1600 cm^{-1} and a broad O-H stretching band near 3400 cm^{-1}, indicating surface hydroxyl groups (Fig 2a). These key peaks in the Fe-doped ZnO spectrum show shifts and reduced intensities, indicating structural modifications caused by iron incorporation [27]. The changes in the Zn-O and Zn-O-Zn bonding regions, as well as the O-H bending and stretching bands, indicate successful Fe integration, which has an effect on the nanocomposite's local bonding environment and surface chemistry (Fig 2b). Such modifications may increase the material's potential for biomedical applications, such as targeted anticancer activity and bio imaging of MCF7 cells.
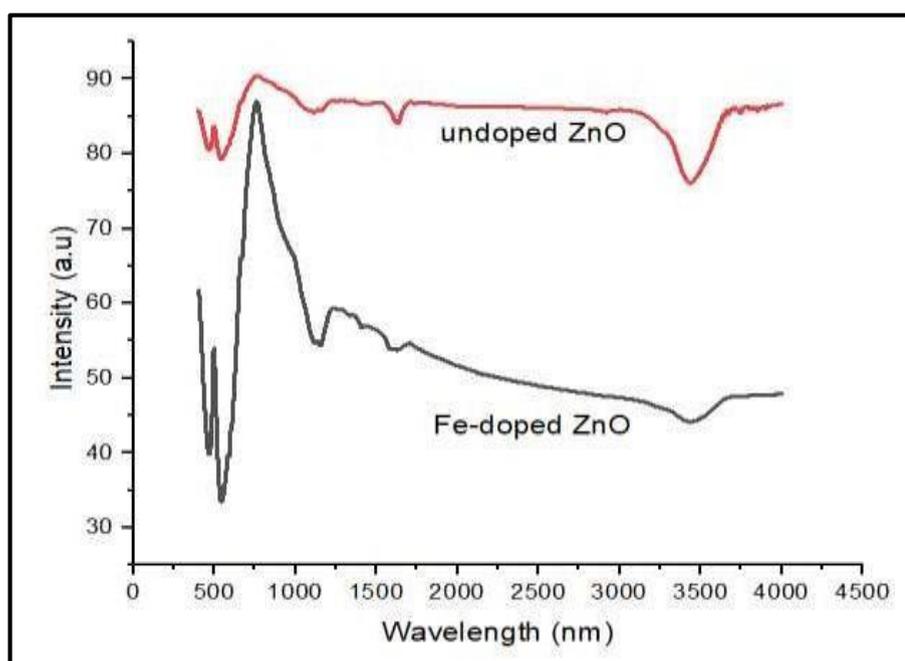

Fig 2: FTIR analysis of Fe-doped ZnO NCs and undoped ZnO NCs

The XRD pattern in Fig 3 compares the crystallographic structures of undoped ZnO and Fe-doped ZnO nanocomposites (Fe-ZnO-NCs). The diffraction peaks are observed in the 2θ range of 10° to 90°, with prominent peaks for Fe-ZnO-NCs appearing around 2θ = 31.7° and 36.3°, representing the (101) and (111) planes, respectively. These peaks indicate ZnO's crystalline structure, with Fe doping significantly increasing peak intensity and crystallinity. The shift in peak positions and increased intensity following Fe doping suggest that Fe ions were successfully incorporated into the ZnO lattice [28]. This doping effect could cause lattice distortions or increase crystallinity, as evidenced by the sharper and more intense peaks in the Fe- ZnO-NCs compared to the undoped sample. Such structural changes imply that Fe-ZnO-NCs has a different lattice environment, potentially improving its electronic and surface properties, which could be useful in catalysis, sensing, and biomedical applications. The absence of secondary peaks indicates that the Fe-ZnO-NCs are phase pure, confirming that Fe incorporation does not result in the formation of new crystalline phases.
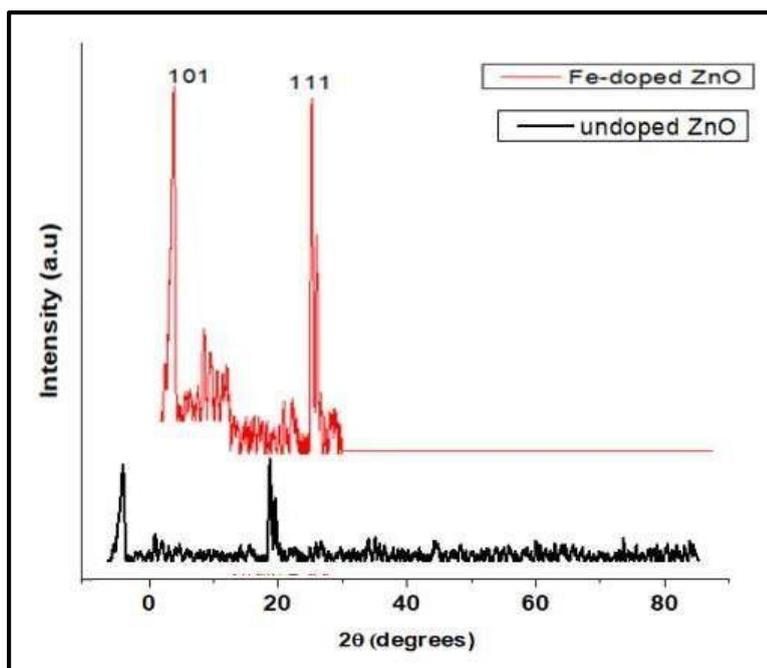
Fig 3: XRD pattern of Fe-doped ZnO-NCs and Undoped ZnO NCs

HRTEM images show the morphology and nanostructure of Fe-doped ZnO nanocomposites (Fe-ZnO-NCs). Fig 4a, taken at lower magnification (scale bar = 50 nm), depicts the formation of well-defined, polyhedral ZnO nanoparticles with an average size of around 50 nm. The particles have clear edges and boundaries, indicating good crystallinity and a uniform size distribution throughout the sample. Some darker regions within the particles may indicate the presence of Fe atoms or minor differences in particle density due to doping. Fig 4b, taken at a higher magnification (scale bar = 10 nm), shows the detailed lattice structure of Fe-doped ZnO. The visible lattice fringes confirm the material's crystalline nature, with interplanar spacing that corresponds to ZnO's wurtzite crystal structure. The high-resolution image also shows minimal lattice distortions, indicating that Fe ions can be effectively incorporated into the ZnO matrix while maintaining crystallinity [29]. Because of their improved surface and electronic properties, Fe- doped ZnO nanocomposites have a greater potential for applications in catalysis, sensing, and biomedicine.
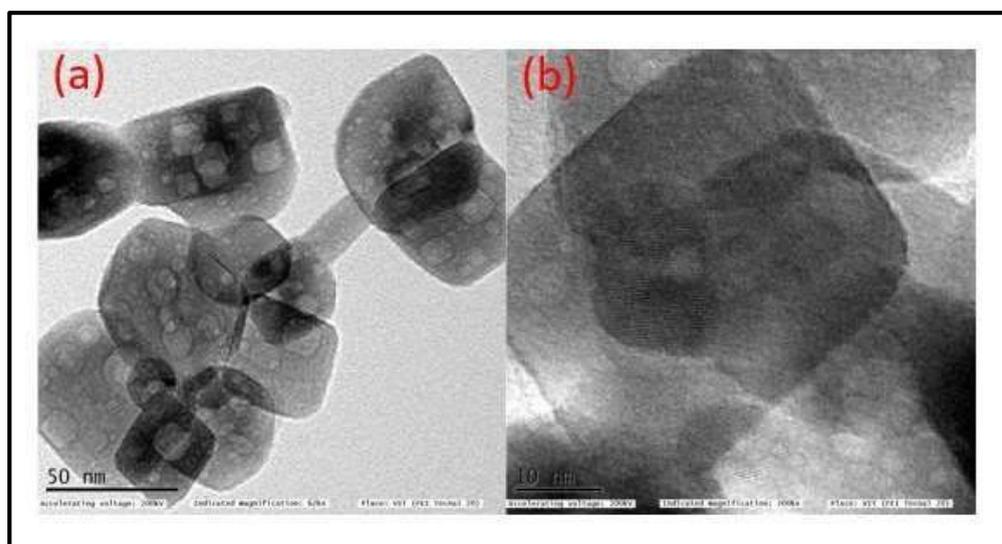

Fig 4: HRTEM images of undoped ZnO NCs and Fe-doped ZnO NCs

The HRSEM images show the surface morphology of ZnO-NCs, comparing undoped ZnO (Fig 5a) to Fe-ZnO-NCs (Fig 5b). Figure 5a depicts the undoped ZnO nanocomposite, which has a relatively smooth distribution of ZnO particles across the biopolymer matrix, with visible clusters and agglomerates. The surface texture indicates that ZnO nanoparticles were homogeneously integrated into the biopolymer structure. In Fig 5b, the Fe-ZnO-NCs show more pronounced roughness and particle density, with the doped sample having a denser, more granular surface than the undoped version. This increased roughness and particle aggregation could be attributed to the presence of iron, which may influence particle formation and distribution within the biopolymer matrix [30]. The addition of iron to the ZnO structure is likely intended to improve the nanocomposite's multifunctional properties, potentially increasing its effectiveness in applications such as anticancer activity and imaging, with a focus on MCF-7 breast cancer cells. The morphological differences between undoped and Fe-doped ZnO indicate that doping can significantly alter the nanocomposite's structural characteristics, potentially improving biological interactions and functional properties.
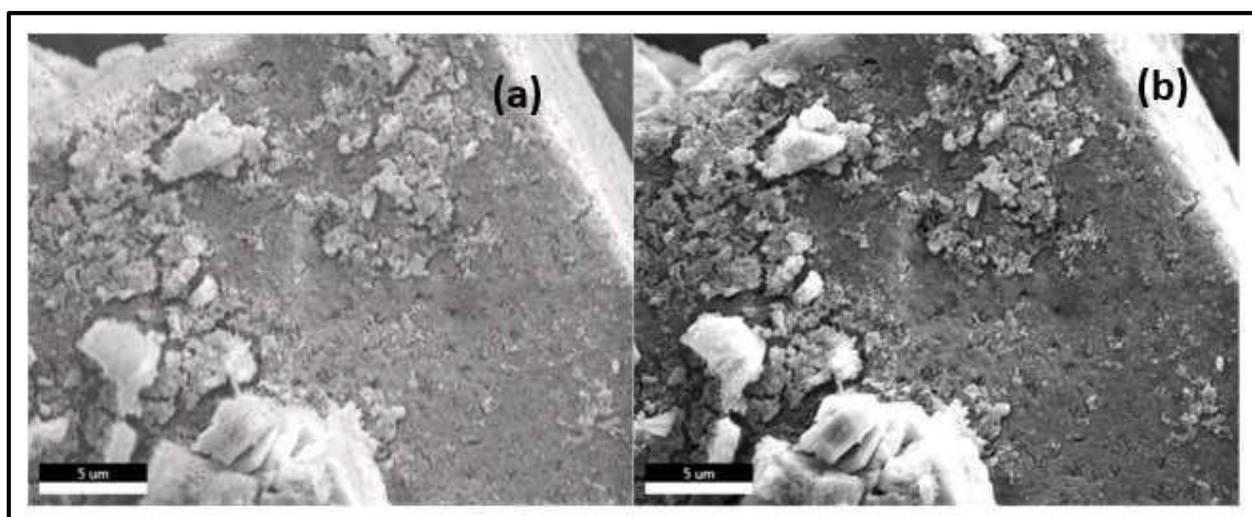

Fig 5: HR SEM of undoped ZnO NCs and Fe-doped ZnO NCs

An Energy Dispersive X-ray (EDX) spectrum of Fe-ZnO-NCs made from *birch* leaf biopolymers is displayed in Fig 6. The Fe-ZnO-NCs sample's elemental composition is revealed by this EDX analysis. Since carbon (C) and oxygen (O) are important components of organic biopolymers, the *birch* leaf-derived biopolymer matrix is probably the cause of the spectrum's prominent peaks for these elements [31]. The successful doping of ZnO with iron is confirmed by the presence of a small peak for iron (Fe), which shows that Fe atoms are integrated into the ZnO structure. The spectrum's lack of any notable impurity peaks indicates that iron was successfully added to the ZnO matrix by the synthesis process without the introduction of undesirable impurities. The possible use of the Fe-ZnO-NCs is supported by this elemental composition.
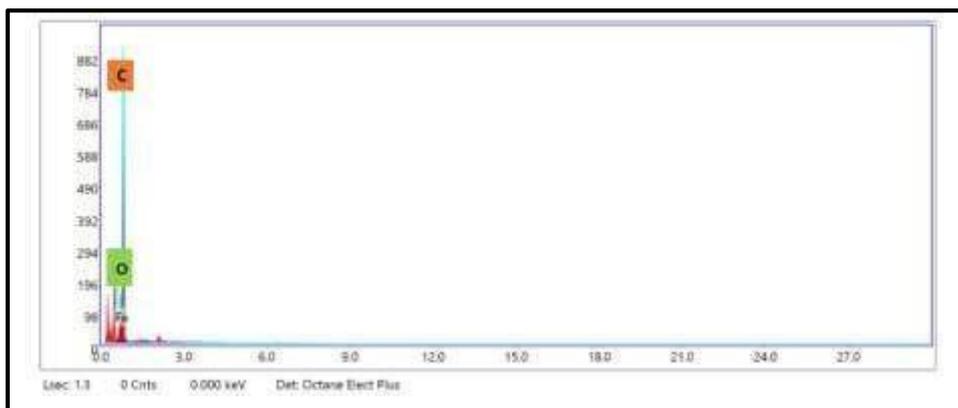
Fig 6: EDX spectra of Fe-Doped ZnO NCs

Fig 7 illustrates nitrogen adsorption-desorption measurements using a Brunauer–Emmett–Teller (BET) isotherm plot for Fe-doped ZnO and undoped ZnO. The surface area, pore structure, and adsorption properties of the doped and undoped ZnO nanocomposites are revealed by this plot. As is common for mesoporous materials, the isotherms for Fe-ZnO-NCs and undoped ZnO display Type IV features with a hysteresis loop. In comparison to undoped ZnO, the Fe-ZnO-NCs exhibit a larger adsorption volume, indicating that iron doping has enhanced the ZnO nanocomposite's surface area and/or porosity. Because it provides more active sites for interactions, this increased surface area may be advantageous for uses in drug delivery, adsorption, and catalysis [32]. For the Fe-ZnO-NCs, the hysteresis loop is more noticeable, suggesting that the addition of iron alters the pore structure and may result in larger or more interconnected pores in the material. These variations in the adsorption behaviour of undoped ZnO and Fe-ZnO-NCs demonstrate how iron doping affects the material's structural characteristics, which can enhance its performance in a range of environmental and biomedical applications.
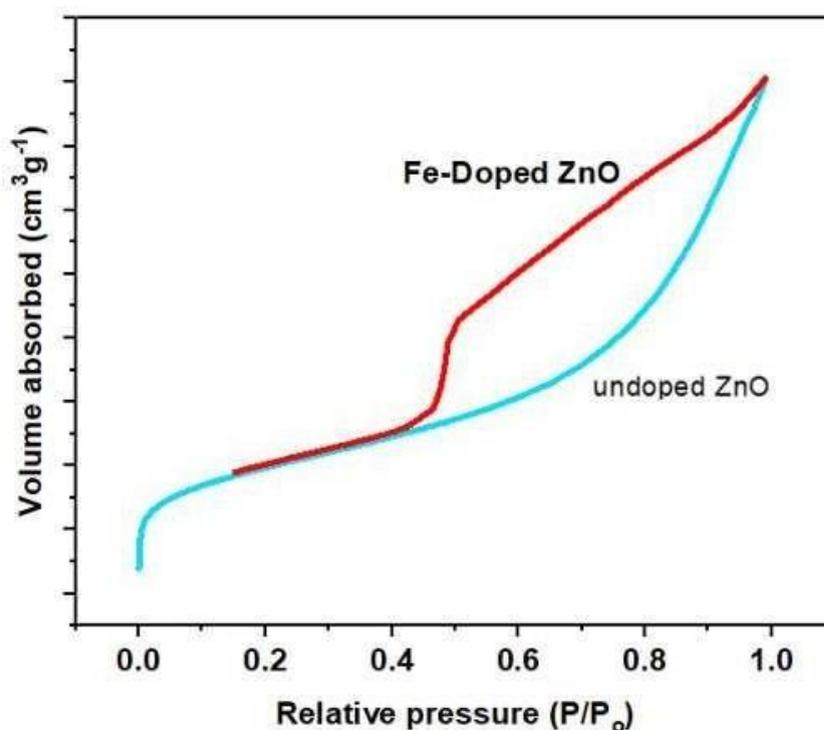

Fig 7: BET analysis of Fe-Doped ZnO NCs and Undoped ZnO NCs

The properties of undoped and Fe-doped (iron-doped) zinc oxide (ZnO) nanocomposites made from *birch* leaf biopolymers are analysed in two graphs in Figure 8. The particle size distribution is shown on the left in Fig. 8a. The intensity of the undoped ZnO is higher than that of the Fe-ZnO-NCs, which also peaks at about 100 nm but with a slightly lower intensity. This implies that particle size distribution is influenced by iron doping. Figure 8b shows the zeta potential. Though the undoped ZnO exhibits a marginally higher frequency percentage than the Fe-ZnO-NCs, both undoped and Fe-ZnO-NCs have comparable patterns, peaking at about -20 mV. This suggests that doping has an impact on the distribution of surface charges, which could affect the stability and cell-nanoparticle interaction [33]. According to these analyses, Fe-doping alters the zeta potential and particle size, which may have an impact on the nanocomposites' efficacy in imaging and cancer treatment applications.
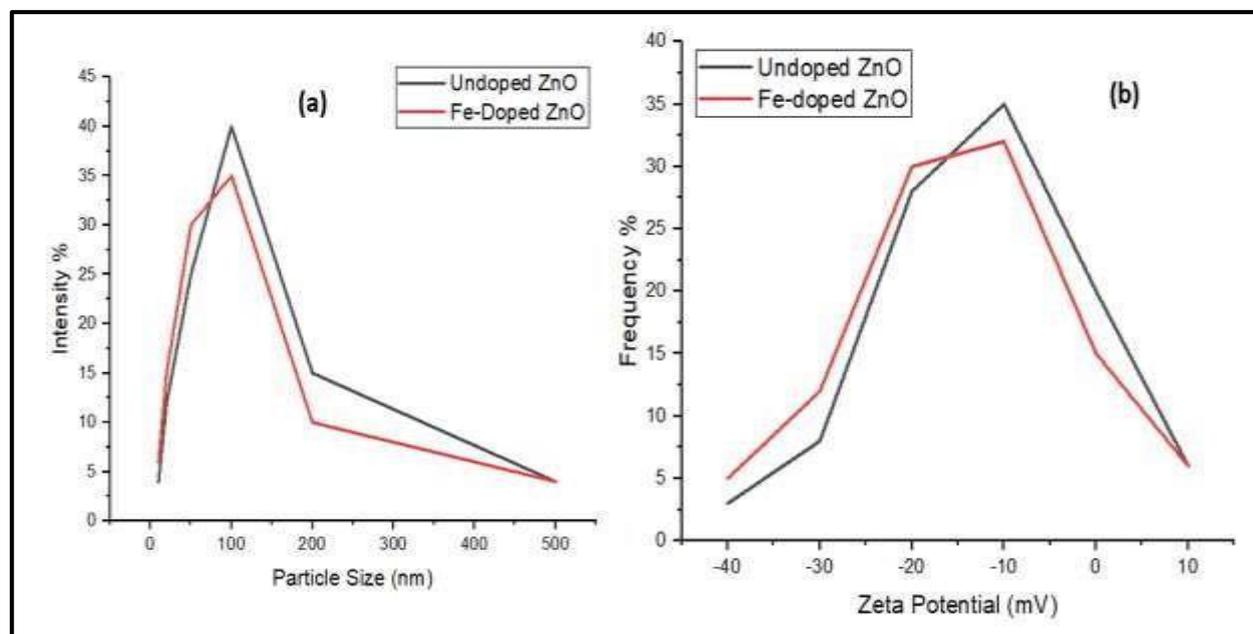

Fig 8: (a) Particle size and (b) Zeta potential analysis of Fe-Doped ZnO NCs and Undoped ZnO NCs

3.2. Anticancer Activity

In terms of cell viability percentage, Fig. 9 compares the cytotoxic effects of undoped ZnO and Fe-ZnO-NCs on MCF-7 breast cancer cells at different concentrations (0, 10, 25, 50, 100, and 200 µg/mL). Both the undoped and Fe-ZnO-NCs treatments exhibit a pronounced dose-dependent decrease in cell viability, with the Fe-ZnO-NCs treatment showing a noticeably larger decline. Undoped ZnO exhibits moderate cytotoxic effects at lower concentrations (10 and 25 µg/mL), lowering cell viability to about 85% and 70%, respectively. Fe-ZnO-NCs, on the other hand, cause a more dramatic decrease, lowering viability to about 75% and 60% at the same concentrations. The two groups' differences become more noticeable as the concentration rises to 50, 100, and 200 µg/mL. For example, undoped ZnO reduces viability to about 50% at 50 µg/mL, whereas Fe-ZnO-NCs reduces it to about 40%. This suggests a much stronger cytotoxic effect, about 1.25 times greater than that of undoped ZnO. Undoped ZnO and Fe-doped ZnO treatments reduce cell viability to about 20% and 10%, respectively, at the highest concentration (200 µg/mL). At this dose, Fe-ZnO-NCs show almost total eradication of cell viability, which is about two times more cytotoxic than undoped ZnO. In Fig.10 phase contrast microscopic images corroborate these. This significant difference emphasizes Fe-doped ZnO's improved anticancer potential, most likely as a result of increased ROS generation made possible by the Fe content, which more successfully induces apoptosis through

oxidative stress mechanisms [34]. The general pattern emphasizes how Fe doping increases ZnO's cytotoxic qualities, making it a stronger contender for anticancer uses.
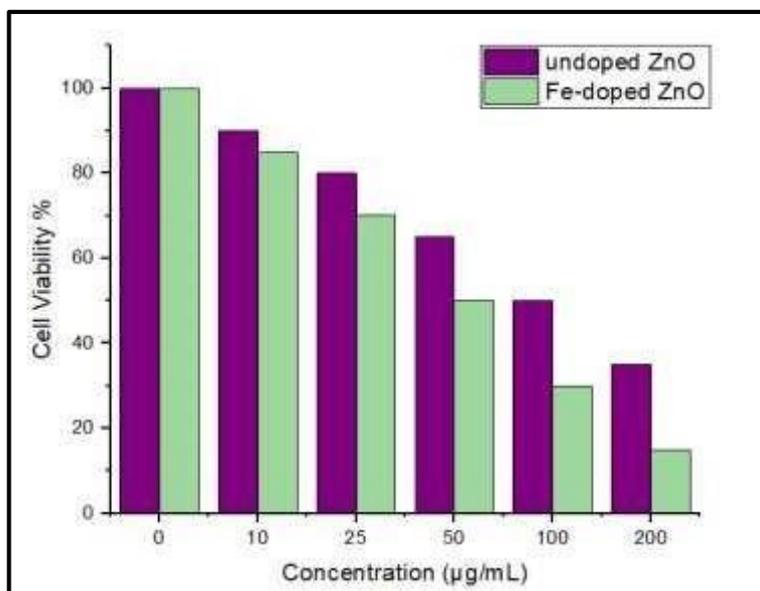

Fig 9: Cell viability of MCF-7 breast cancer cells treated with undoped and Fe-doped ZnO at concentrations from 0 to 200 µg/mL. Fe-doped ZnO shows significantly greater cytotoxicity, decreasing cell viability more effectively in a dose-dependent manner.
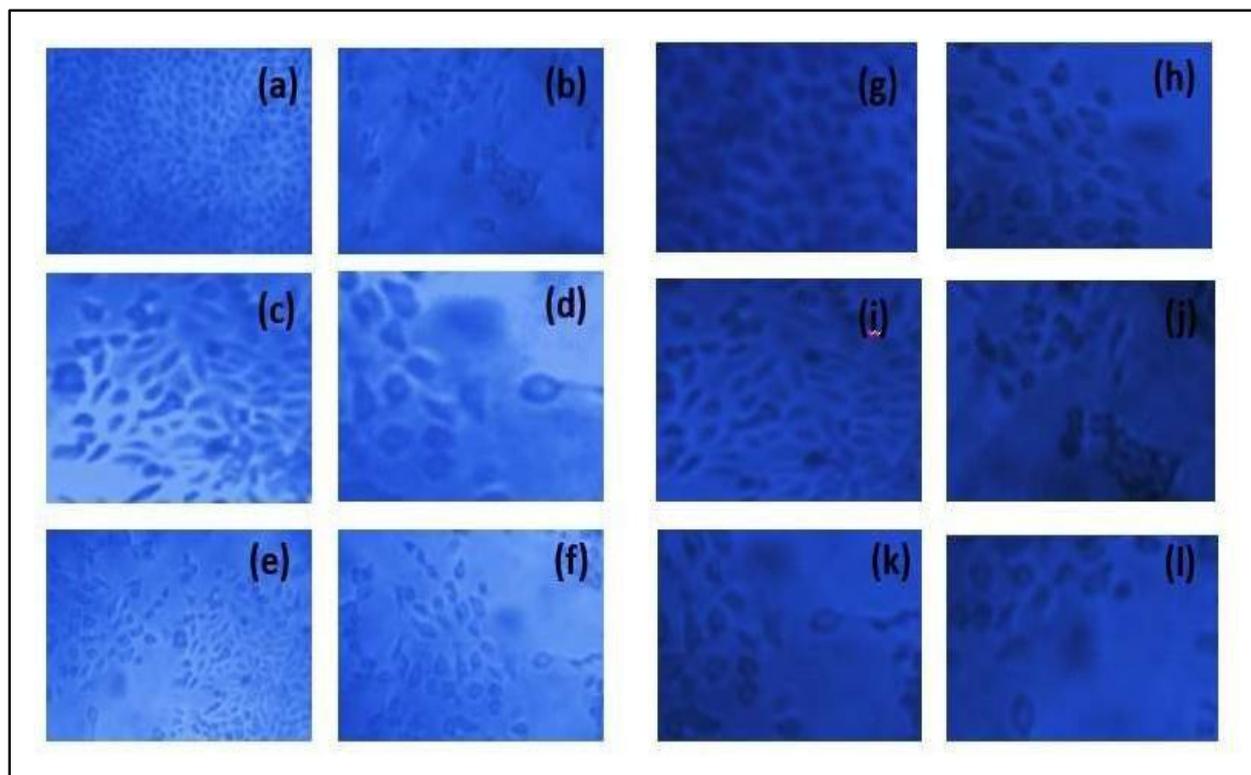

Fig 10: Microscopic images of MCF-7 cells treated with undoped (a-f) and Fe-doped ZnO (g-l) at 0, 10, 25, 50, 100, and 200 µg/mL. Fe-doped ZnO causes more cell shrinkage and detachment, indicating stronger cytotoxic effects.

3.3. Apoptotic Effects of Fe-doped ZnO Nanoparticles via ROS Generation and Mitochondrial Disruption

Fe-doped ZnO nanoparticles' effects on cellular apoptosis, ROS production, and mitochondrial membrane potential (MMP) disruption are thoroughly examined in Fig. 11 in comparison to undoped ZnO and control conditions. To clarify the function of Fe-doped ZnO in promoting cellular apoptosis, the study combines fluorescence measurements, Western blot analysis, and apoptosis assays. The percentage of apoptotic cells classified as early, late, and total apoptosis is assessed for three treatment groups: Control, undoped ZnO, and Fe-ZnO-NCs, in the apoptosis assay (Fig 11a). Fe-ZnO-NCs exhibit the highest overall apoptosis among the groups due to a significant increase in both early and late apoptosis rates. This pattern implies that Fe-ZnO-NCs, as opposed to undoped ZnO and control treatments, are more successful in causing cell death via apoptosis pathways [35].

By analysing the expression levels of apoptosis-related markers, particularly Bax, Caspases, and Bcl-2, the Western blot analysis (Fig 11b) provides additional support for these conclusions. An increased activation of apoptosis pathways is indicated by the significant upregulation of the pro-apoptotic markers Bax and Caspases in the Fe-doped ZnO group. The anti-apoptotic marker Bcl-2, on the other hand, is downregulated in cells treated with Fe-ZnO-NCs, indicating that Fe-ZnO-NCs promotes apoptosis by blocking anti-apoptotic signalling. Reactive oxygen species (ROS) levels under each treatment condition are shown in Fig. 11c, expressed as relative fluorescence units. The highest ROS levels are produced by the Fe-doped ZnO treatment, which significantly outperforms the undoped ZnO and control groups. This rise in ROS indicates that Fe-ZnO-NCs cause oxidative stress in the cells, which is a crucial element frequently linked to the induction of apoptosis. The MMP disruption data further supports the possibility that mitochondrial dysfunction is linked to elevated ROS levels. The disruption of the mitochondrial membrane potential (MMP) is evaluated in Fig. 11d. With a significant decrease in Undoped ZnO and a further decline in the Fe-ZnO-NCs group, the control group shows the highest MMP. Significant MMP disruption in cells treated with Fe-ZnO-NCs suggests impaired mitochondrial integrity, which is a sign of the start of apoptosis. The observed apoptotic cell death in the Fe-ZnO-NCs group is probably caused by the combined effects of increased ROS and MMP loss. Fe-ZnO-NCs exhibit a strong pro-apoptotic effect via a complex mechanism that includes mitochondrial disruption, upregulation of pro-apoptotic markers, and increased ROS production [36–37]. These results imply that Fe-ZnO-NCs may be a useful tool for causing target cells to undergo apoptosis, which may be necessary for therapeutic uses involving targeted cell death.
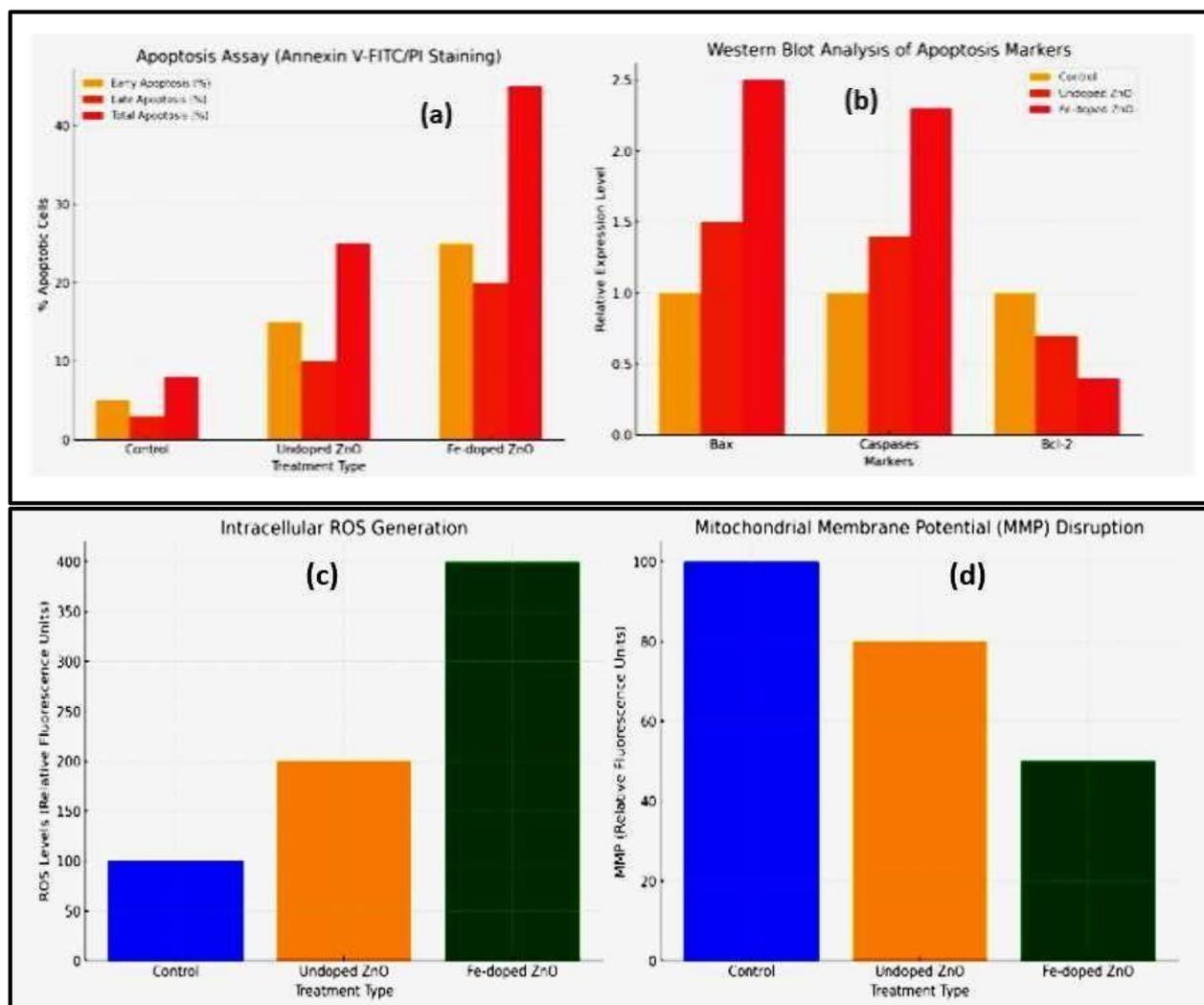
Fig 11: Effects of Fe-doped ZnO nanoparticles on cellular apoptosis and oxidative stress.
(a) Apoptosis assay showing early, late, and total apoptosis percentages.
(b) Western blot analysis of apoptotic markers (Bax, Caspases, Bcl-2) under different treatments.
(c) Intracellular ROS levels indicating oxidative stress induction.
(d) Mitochondrial membrane potential (MMP) disruption, highlighting mitochondrial integrity loss.

3.4. Imaging Capabilities

Fig 12 illustrates the enhancement brought about by Fe-doping with particular values by comparing Fe-doped ZnO with undoped ZnO across three properties: T2 relaxivity, X-ray intensity, and Hounsfield Units. Each property is measured over a concentration range of 0 to 10 mg/mL. In contrast to undoped ZnO, which levels off at about 60 s^{-1} mM^{-1} after 2 mg/mL, the T2 relaxivity (s^{-1} mM^{-1}) of Fe-doped ZnO increases dramatically in Fig. 12a, reaching about 150 s^{-1} mM^{-1} at 10 mg/mL. This implies that Fe-doping greatly increases T2 relaxivity, which strengthens the case for Fe-doped ZnO as an MRI contrast agent. The X-ray intensity (AU) is shown in Fig 12b. At the highest concentration, Fe-doped ZnO exhibits a continuous increase to about 80 AU, whereas undoped ZnO stays almost flat at about 10 AU at all concentrations. This significant variation implies that Fe-doped ZnO offers significantly improved contrast for X-ray imaging. Hounsfield Units (HU) rise with concentration for both Fe-doped and undoped ZnO in Fig. 12c, but at 10 mg/mL, Fe-doped ZnO reaches about 450 HU while undoped ZnO only reaches about 300 HU at the same concentration [38]. Fe-doped ZnO has better radiodensity, which increases its visibility

in CT imaging, according to the higher HU values. Fe-doped ZnO is a more effective contrast agent for multimodal imaging applications because it performs better overall than undoped ZnO across all measured properties, with particular values showing significantly improved T2 relaxivity, X-ray intensity, and Hounsfield Units.
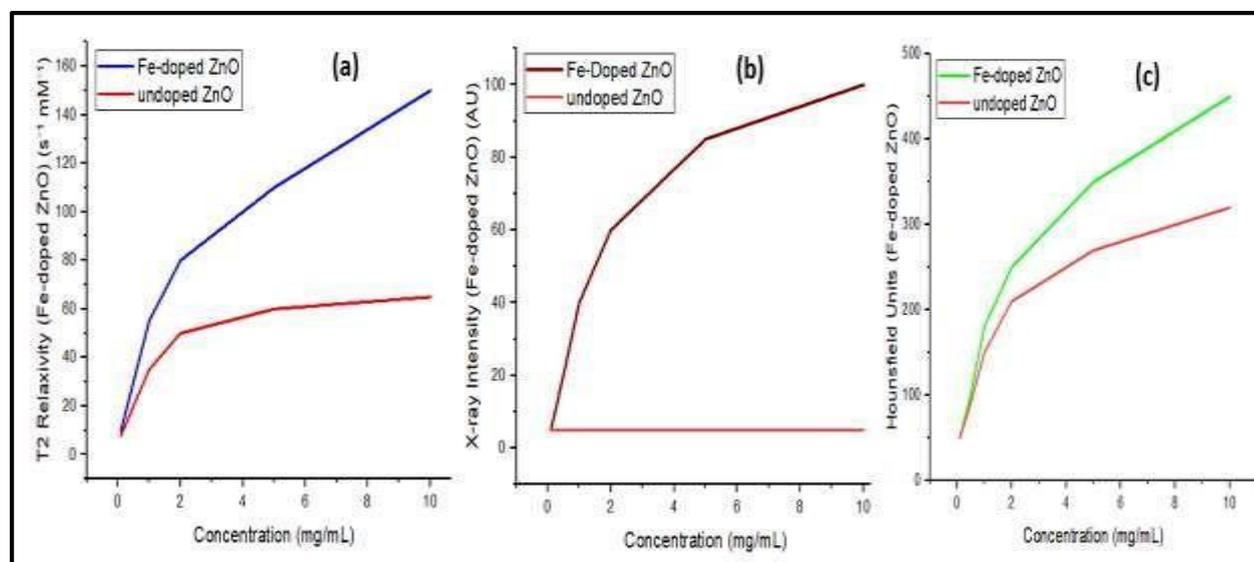

Fig 12: Comparative imaging properties of Fe-doped ZnO vs undoped ZnO across concentrations. (a) T2 relaxivity peaks at ~150 s^{-1} mM^{-1} for Fe-doped ZnO, versus ~60 s^{-1} mM^{-1} for undoped ZnO. (b) X-ray intensity reaches ~80 AU for Fe-doped ZnO, remaining ~10 AU for undoped ZnO. (c) Hounsfield Units (HU) for Fe-doped ZnO reach 450, compared to 300 for undoped ZnO, indicating Fe-doped ZnO's enhanced suitability for multimodal imaging.

4. CONCLUSION

Birch leaf biopolymers are used to create iron-doped zinc oxide (Fe-ZnO) nanocomposites, which show great promise as multipurpose platforms for cancer theranostics that target breast cancer cells in particular. Fe-ZnO nanocomposites demonstrate improved stability, surface characteristics, and a morphology that is optimized through thorough structural and functional characterization. These attributes are critical for biomedical applications. With increased ROS generation and apoptosis induction, iron greatly increases ZnO's anticancer efficacy, making Fe-ZnO a powerful cytotoxic agent against cancer cells. Because of the magnetic and radiopaque qualities that iron doping imparts, Fe-ZnO nanocomposites offer strong imaging capabilities across MRI, X-ray, and CT modalities in addition to their therapeutic advantages. Fe-ZnO can be used both therapeutically and diagnostically at the same time thanks to its dual functionality, which makes it a potent theranostic agent for integrated cancer management. These results highlight the potential and adaptability of Fe-ZnO nanocomposites in the treatment of cancer, providing a platform that permits real-time therapeutic effect monitoring. Along with investigating targeted delivery methods, more in vivo research is advised to confirm biocompatibility and therapeutic efficacy in animal models. These kinds of advancements are necessary to move Fe-ZnO nanocomposites closer to clinical use, where they may offer a novel way to diagnose and treat breast cancer simultaneously.

REFERENCES

1. Khursheed, R., Dua, K., Vishwas, S., Gulati, M., Jha, N. K., Aldhafeeri, G. M & Singh, S. K. (2022). Biomedical applications of metallic nanoparticles in cancer: Current status and future perspectives. Biomedicine & pharmacotherapy, 150, 112951.
2. Kim, D., Shin, K., Kwon, S. G., & Hyeon, T. (2018). Synthesis and biomedical applications of multifunctional nanoparticles. Advanced Materials, 30(49), 1802309.
3. Subbiah, R., Veerapandian, M., & S. Yun, K. (2010). Nanoparticles: functionalization and multifunctional applications in biomedical sciences. Current medicinal chemistry, 17(36), 4559-4577.
4. Kim, D., Shin, K., Kwon, S. G., & Hyeon, T. (2018). Synthesis and biomedical applications of multifunctional nanoparticles. Advanced Materials, 30(49), 1802309.
5. Parvanian, S., Mostafavi, S. M., & Aghashiri, M. (2017). Multifunctional nanoparticle developments in cancer diagnosis and treatment. Sensing and Bio-Sensing Research, 13, 81-87.
6. Gu, Z., Zhu, S., Yan, L., Zhao, F., & Zhao, Y. (2019). Graphene-based smart platforms for combined Cancer therapy. Advanced Materials, 31(9), 1800662.
7. Govindan, B., Sabri, M. A., Hai, A., Banat, F., & Haija, M. A. (2023). A review of advanced multifunctional magnetic nanostructures for cancer diagnosis and therapy integrated into an artificial intelligence approach. Pharmaceutics, 15(3), 868.
8. Kalimuthu, K., Cha, B. S., Kim, S., & Park, K. S. (2020). Eco-friendly synthesis and biomedical applications of gold nanoparticles: A review. Microchemical Journal, 152, 104296.
9. Soufi, G. J., & Iravani, S. (2020). Eco-friendly and sustainable synthesis of biocompatible nanomaterials for diagnostic imaging: current challenges and future perspectives. Green Chemistry, 22(9), 2662-2687.
10. Chen, H., Rogalski, M. M., & Anker, J. N. (2012). Advances in functional X-ray imaging techniques and contrast agents. Physical Chemistry Chemical Physics, 14(39), 13469-13486.
11. Huang, W. Y., & Davis, J. J. (2011). Multimodality and nanoparticles in medical imaging. Dalton Transactions, 40(23), 6087-6103.
12. Cisneros-Yupanqui, M., Chalova, V. I., Kalaydzhiev, H. R., Mihaylova, D., Krastanov, A. I., & Lante, A. (2023). Ultrasound-assisted extraction of antioxidant bioactive compounds from wastes of rapeseed industry and their application in delaying rapeseed oil oxidation. Environmental Technology & Innovation, 30, 103081.
13. Sharma, P., & Sharma, P. (2020). Assessment of the antimicrobial and antioxidant activity of oil seed meals against food-borne pathogens, and their application in poultry meat product (Doctoral dissertation, Naresuan University).
14. Kamalidehghan, B., Houshmand, M., Kamalidehghan, F., Jafarzadeh, N., Azari, S., Akmal, S. N., & Rosli, R. (2012). Establishment and characterization of two human breast carcinoma cell lines by spontaneous immortalization: Discordance between Estrogen, Progesterone and HER2/neu receptors of breast carcinoma tissues with derived cell lines. Cancer cell international, 12, 1-15.
15. Abaza, A., Mahmoud, G. A., Hegazy, E. A., Amin, M., Shoukry, E., & Elsheikh, B. (2018). Cytotoxic effect of chitosan based nanocomposite synthesized by radiation: in vitro liver and breast cancer cell line. Journal of Pharmacy and Pharmacology, 6, 305-319.
16. Atif, M., Iqbal, S., Fakhar-E-Alam, M., Ismail, M., Mansoor, Q., Mughal, L & Farooq, W. A. (2019). Manganese-Doped Cerium Oxide Nanocomposite Induced Photodynamic Therapy in MCF-7 Cancer Cells and Antibacterial Activity. BioMed Research International, 2019(1), 7156828.
17. Vistica, D. T., Skehan, P., Scudiero, D., Monks, A., Pittman, A., & Boyd, M. R. (1991). Tetrazolium-based assays for cellular viability: a critical examination of selected parameters affecting formazan production. Cancer research, 51(10), 2515-2520.
18. Stockert, J. C., Blázquez-Castro, A., Cañete, M., Horobin, R. W., & Villanueva, Á. (2012). MTT assay for cell viability: Intracellular localization of the formazan product is in lipid droplets. Acta histochemica, 114(8), 785-796.
19. Chen, S., Cheng, A. C., Wang, M. S., & Peng, X. (2008). Detection of apoptosis induced by new type gosling viral enteritis virus in vitro through fluorescein annexin V-FITC/PI double labeling. World Journal of Gastroenterology: WJG, 14(14), 2174.
20. Uusitalo, L. M., & Hempel, N. (2012). Recent advances in intracellular and in vivo ROS sensing: focus on nanoparticle and nanotube applications. International journal of molecular sciences, 13(9), 10660-10679.

21. Shen, B., He, P. J., & Shao, C. L. (2013). Norcantharidin induced DU145 cell apoptosis through ROS-mediated mitochondrial dysfunction and energy depletion. PloS one, 8(12), e84610.

22. Fatahi, M., & Speck, O. (2015). Magnetic resonance imaging (MRI): A review of genetic damage investigations. Mutation Research/Reviews in Mutation Research, 764, 51-63.

23. Reda, R., Zanza, A., Mazzoni, A., Cicconetti, A., Testarelli, L., & Di Nardo, D. (2021). An update of the possible applications of magnetic resonance imaging (MRI) in dentistry: a literature review. Journal of imaging, 7(5), 75.

24. Arnone, D., Cavanagh, J., Gerber, D., Lawrie, S. M., Ebmeier, K. P., & McIntosh, A. M. (2009). Magnetic resonance imaging studies in bipolar disorder and schizophrenia: meta-analysis. The British Journal of Psychiatry, 195(3), 194-201.

25. Kitayama, N., Vaccarino, V., Kutner, M., Weiss, P., & Bremner, J. D. (2005). Magnetic resonance imaging (MRI) measurement of hippocampal volume in posttraumatic stress disorder: a meta-analysis. Journal of affective disorders, 88(1), 79-86.

26. Safdar, M. F., Alkobaisi, S. S., & Zahra, F. T. (2020). A comparative analysis of data augmentation approaches for magnetic resonance imaging (MRI) scan images of brain tumor. Acta informatica medica, 28(1), 29.

27. Sahai, A., Kumar, Y., Agarwal, V., Olive-Méndez, S. F., & Goswami, N. (2014). Doping concentration driven morphological evolution of Fe doped ZnO nanostructures. Journal of Applied Physics, 116(16).

28. Ahmed, F., Kumar, S., Arshi, N., Anwar, M. S., & Koo, B. H. (2012). Morphological evolution between nanorods to nanosheets and room temperature ferromagnetism of Fe-doped ZnO nanostructures. CrystEngComm, 14(11), 4016-4026.

29. Saleh, R., Prakoso, S. P., & Fishli, A. (2012). The influence of Fe doping on the structural, magnetic and optical properties of nanocrystalline ZnO particles. Journal of Magnetism and Magnetic Materials, 324(5), 665-670.

30. Wu, X., Wei, Z., Zhang, L., Wang, X., Yang, H., & Jiang, J. (2014). Optical and magnetic properties of Fe doped ZnO nanoparticles obtained by hydrothermal synthesis. Journal of Nanomaterials, 2014(1), 792102.

31. Saqib, A. N. S., Huong, N. T. T., Kim, S. W., Jung, M. H., & Lee, Y. H. (2021). Structural and magnetic properties of highly Fe-doped ZnO nanoparticles synthesized by one-step solution plasma process. Journal of Alloys and Compounds, 853, 157153.

32. Kumar, S., Tiwari, N., Jha, S. N., Chatterjee, S., Bhattacharyya, D., Sahoo, N. K., & Ghosh, A. K. (2015). Insight into the origin of ferromagnetism in Fe-doped ZnO diluted magnetic semiconductor nanocrystals: an EXFAS study of local structure. RSC advances, 5(115), 94658-94669.

33. Yi, S., Cui, J., Li, S., Zhang, L., Wang, D., & Lin, Y. (2014). Enhanced visible-light photocatalytic activity of Fe/ZnO for rhodamine B degradation and its photogenerated charge transfer properties. Applied surface science, 319, 230-236.

34. Kabir, F., Murtaza, A., Saeed, A., Ghani, A., Ali, A., Khan, S., ... & Yang, S. (2022). Structural, optical and magnetic behavior of (Pr, Fe) co-doped ZnO based dilute magnetic semiconducting nanocrystals. Ceramics International, 48(14), 19606-19617.

35. Bilgin, V., Sarica, E., Demirselcuk, B., & Turkyilmaz, S. (2018). Iron doped ZnO thin films deposited by ultrasonic spray pyrolysis: structural, morphological, optical, electrical and magnetic investigations. Journal of Materials Science: Materials in Electronics, 29, 17542-17551.

36. Javed, M., Amjad, A., Iqbal, S., Mahmood, S., Raza, H., Riaz, M & Alshalwi, M. (2024). Engineering the nanostructure of iron-doped ZnO for the construction of Fe-ZnO/SGCN nanocomposites to enhance the spatial charge separation and their potential applications. Materials Science and Engineering: B, 299, 117020.

37. Yu, J., Zhu, F., Yang, Y., Zhang, P., Zheng, Y., Chen, H., & Gao, Y. (2023). Ultrasmall iron-doped zinc oxide nanoparticles for ferroptosis assisted sono-chemodynamic cancer therapy. Colloids and Surfaces B: Biointerfaces, 232, 113606.

38. Mehmood, F., Iqbal, J., Jan, T., & Mansoor, Q. (2017). Structural, Raman and photoluminescence properties of Fe doped WO3 nanoplates with anti-cancer and visible light driven photocatalytic activities. Journal of Alloys and Compounds, 728, 1329-1337.